

Tidal fragmentation as the origin of 1I/2017 U1 (‘Oumuamua)

Yun Zhang^{1,2,3,4*} & Douglas N.C. Lin^{5,2}

¹*National Astronomical Observatories, Chinese Academy of Sciences, Beijing, China.*

²*Institute for Advanced Studies, Tsinghua University, Beijing, China.*

³*Université Côte d’Azur, Observatoire de la Côte d’Azur, CNRS, Laboratoire Lagrange, Nice, France.*

⁴*Department of Astronomy, University of Maryland, College Park, MD, USA.*

⁵*Department of Astronomy and Astrophysics, University of California, Santa Cruz, CA, USA.*

**To whom correspondence should be addressed; Email: yun.zhang@oca.eu*

The first discovered interstellar object (ISO), ‘Oumuamua (1I/2017 U1) shows a dry and rocky surface, an unusually elongated short-to-long axis ratio $c/a \lesssim 1/6$, a low velocity relative to the local standard of rest ($\sim 10 \text{ km s}^{-1}$), non-gravitational accelerations, and tumbles on a few hours timescale¹⁻⁹. The inferred number density ($\sim 3.5 \times 10^{13} - 2 \times 10^{15} \text{ pc}^{-3}$) for a population of asteroidal ISOs^{10,11} outnumber cometary ISOs¹² by $\geq 10^3$, in contrast to the much lower ratio ($\lesssim 10^{-2}$) of rocky/icy Kuiper belt objects¹³. Although some scenarios can cause the ejection of asteroidal ISOs^{14,15}, a unified formation theory has yet to comprehensively link all ‘Oumuamua’s puzzling characteristics and to account for the population. Here we show by numerical simulations that ‘Oumuamua-like ISOs can be prolifically produced through extensive tidal fragmentation and ejected during close encounters of their volatile-rich parent bodies with their host stars. Material strength enhanced by the intensive heating during periastron passages enables the emergence of extremely elongated triaxial ISOs with shape $c/a \lesssim 1/10$, sizes $a \sim 100 \text{ m}$, and rocky surfaces. Although volatiles with low sublimation temperature (such as CO) are concurrently depleted, H₂O buried under surfaces is preserved in these ISOs, providing an outgassing source without measurable cometary activities for ‘Oumuamua’s non-gravitational accelerations during its passage through the inner Solar System. We infer that the progenitors of ‘Oumuamua-like ISOs may be km-sized long-period comets from Oort clouds, km-sized residual planetesimals from debris disks, or planet-size bodies at a few AU, orbiting around low-mass main-sequence stars or white dwarfs. These

provide abundant reservoirs to account for ‘Oumuamua’s occurrence rate.

We use the PKDGRAV N -body code to simulate the tidal disruption processes (see Methods). ‘Oumuamua’s parent bodies are modelled as self-gravitating rubble piles, which represent the most typical structure for Solar System small bodies^{16,17}. A soft-sphere discrete-element model is applied to compute the contact forces and torques between granules in the normal, tangential, rolling, and twisting directions. These quantities determine the magnitude of the material shear and cohesive strengths. For the first set of models, the parent body is represented as a spherical granular aggregate with an initial bulk density of $\rho_p = 2,000 \text{ kg m}^{-3}$, a radius of $R_p = 100 \text{ m}$, and no initial spin. The host is assumed to be a main-sequence star whose mass $M_s = 0.5M_\odot$, radius $R_s \simeq 0.5R_\odot$, and average density $\rho_s \simeq 4\rho_\odot$ (the region where tidal disruption occurs is much larger around low-mass stars as they have higher densities; see Methods). Its limiting distance of tidal disruption for gravity-dominated bodies¹⁸ (such as gas giants, super-Earths, minor and dwarf planets) is $d_{\text{limit}}(R_p \gtrsim 1 \text{ km}) = 1.05(M_s/\rho_p)^{1/3} \simeq 8.3 \times 10^8 \text{ m} > R_s$. Small bodies with radii smaller than a few km are bonded by material strength. The limiting distance for these strength-dominated bodies is modified to be $d_{\text{limit}}(R_p \lesssim 1 \text{ km}) \simeq 0.52(C_1/R_p^2\rho_p^2 + C_2)^{-1/3}(M_s/\rho_p)^{1/3}$, where C_1 and C_2 are constants related to the material cohesive and shear strengths, respectively (see Methods). Objects with $d_{\text{limit}}(R_p) \lesssim R_s$ would crash coherently into their host stars if their periastron distance $d_p < R_s$. Accordingly, our simulation results can be scaled to different values of R_p , ρ_p , and M_s .

We performed a series of simulations with the parent body approaches the host star on a high-eccentricity e_0 orbit with $d_p = 3.5\text{--}8.0 \times 10^8 \text{ m} > R_s$. After the tidal disruption, it breaks up into many pieces with fractional $f_E \sim \pm R_p/[(1 - e_0)d_p]$ change to their incoming specific orbital energy. The criterion for a significant fraction of the fragments to escape from the host stars is $|f_E| \gtrsim 1$ or $(1 - e_0) \lesssim R_p/d_p$ (see Methods). For the parent bodies with $R_p = 100 \text{ m}$ considered in the first set of simulations, $(1 - e_0) \sim 10^{-6}$ is required to meet the ejection criterion. The corresponding initial orbital semi-major axis $a_0 = 2,300\text{--}5,300 \text{ AU}$, which is comparable to the size of the inner Oort cloud in the Solar System. The tidal debris of larger- R_p parent bodies can readily escape with smaller e_0 and a_0 . A second set of simulations (see below) on the passage of $R_p = 2 \times 10^7 \text{ m}$ super-Earths with similar periastron distances shows that half of the fragments can be ejected with a smaller $e_0 \sim 0.999$. The corresponding a_0 (a few AU) is within the region

where most planets reside.

As shown in Fig. 1, during the periastron passage, the integrity of the parent body is preserved by its intrinsic material shear strength for encounters with $d_p \gtrsim 6 \times 10^8$ m (see Methods). For closer encounters, the parent body is spun up, significantly distorted and then disrupted by the stellar tides, to produce numerous fragments (see Supplementary Video 1). The tidal force is a steeply decreasing function of the periastron distance. With a smaller d_p , the parent body breaks up into a greater number of smaller, highly elongated fragments (see the top-left insert of Fig. 1 and Supplementary Fig. 1). The normalised orbital-energy-per-mass increment $f_E > 1$ for some fragments. This change is adequate for them to escape (represented by the red fragments in Fig. 1) from the gravitational potential of their host star plus additional, if any, Jupiter-like planets (see Methods).

Nearly all the fragments are triaxial prolate and rapidly tumbling. Larger fragments tend to tumble on timescale of a few to tens of hours with more extreme c/a ratios. The light curve associated with this state is compatible with observations on ‘Oumuamua (see Methods). The timescale of damping their tumbling motion by their internal friction is > 5 Gyr (see Methods). The fragments’ internal density is generally reduced by the tidal and rotational deformation to $\sim \rho_p/2 \sim 1,000$ kg m⁻³. Despite the low density, their internal friction and cohesion (in addition to gravity) prevent them from rotational breakup. In order to consider a range of potential material strengths, we performed tidal disruption simulations with different friction angles ϕ and cohesive strengths C to show that the production of elongated (with $c/a \lesssim 1/3$) fragments is robust (see Fig. 2).

Planetesimal parent bodies originated well outside the snow line (at a few AU) are likely to have icy/rocky composition similar to that of the comets. But, their surfaces are intensely heated by their original host stars during the disruptive periastron passage. The thermal modelling (see Fig. 3 and Methods) shows that the melting and re-condensation (at 3 hours after periastron) of surface silicates lead to the build-up of desiccated crusts on the resulting fragments and the transformation from cometary to asteroidal exteriors. The enhancement of cohesion due to sintering of silicates in the crusts leads to more extreme c/a ($\lesssim 1/10$) with $a \sim 100$ m (see Fig. 2b). These results offer a possible formation scenario for the reported shape, size, and surface features of ‘Oumuamua.

Heat diffusion continues after periastron passage. At 3 m beneath fragments’ surfaces, the temperature may reach 28 K (CO’s sublimation temperature) at 37,000 days after periastron (at ~ 100 AU), such that a substantial fraction of volatiles in an ‘Oumuamua-size fragment may be evaporated. The CO depletion provides an explanation not only for ‘Oumuamua’s spectroscopic properties⁸, but also for the observationally inferred “dryness” (i.e., large rock/ice-ratio compared to cometary material) of the interstellar population^{10,11}. Despite the CO depletion, H₂O and CO₂ (with higher sublimation temperature), buried at depths $> 0.1\text{--}0.2$ m and $> 0.2\text{--}0.5$ m, respectively, remain in a condensed form (see Fig. 3).

After the formation and ejection from their host stars, the fragments’ motion is gravitationally accelerated, dragged by the interstellar gas, and retarded by the interstellar magnetic field through Alfvén propulsion¹⁹. When a dynamical equilibrium is established by the balance of these effects, the ISOs attain a size-dependent terminal speed $v_{\text{term}}(R_{\text{ISO}})$ relative to the local standard of rest (LSR) without significant spin evolution (see Methods). For a 100-m-sized object formed a few Gyr ago, v_{term} is consistent with the observed motion of ‘Oumuamua (~ 10 km s⁻¹) prior to its Solar System entry. This magnetic retardation effect is negligible on ISOs with radii $R_{\text{ISO}} \gtrsim 1$ km and their motion relative to the LSR is expected to be similar to stars with comparable age.

Following ‘Oumuamua’s passage through the inner Solar System, near perihelion, the H₂O sublimation temperature is reached at greater depths beneath the crusts of the fragments than during the course of their prior formation and ejection (see Fig. 3c), as the Sun is brighter and hotter than their original low-mass host star (see Methods). Vaporisation of this additional inventory of volatile may bring some organic material to their porous surfaces with photometric characteristics resembling that found from ‘Oumuamua’s colour analyses²⁰. Despite the lack of coma, the delayed resumption of outgassing may also lead to the reported non-gravitational accelerations^{7,8} (see Methods).

Based on the described formation and ejection mechanism, long-period comets (LPCs) and residual planetesimals on nearly parabolic orbits are promising candidates for ‘Oumuamua’s parent bodies. Under the combined influence of the Galactic tide, passing stars, and planetary perturbations^{21,22}, a few km-sized LPCs intrude each year from the inner Oort cloud (with $a_0 \lesssim 2 \times 10^4$ AU) to the stellar proximity with $1 - e_0 \lesssim 10^{-5}$. Since the size of typical visible comets are much larger

($\gtrsim 10$) than ‘Oumuamua, they can provide an adequate supply of asteroidal ISOs through the accumulative ejection of the extensively downsized tidal fragments (analogous to Shoemaker-Levy-9) from a few percent of the LPC population (comparable to the required mass ejection per star $M_{\text{ej}} \simeq (0.0017\text{--}0.1)M_{\oplus}$; see Methods). Debris disks are common around other stars and they are also potential reservoirs of asteroidal ISOs. Similar physical processes can also lead to cometary ISOs¹¹ through the direct detachment of icy residual planetesimals without tidal disruption and intense heating in the proximity of their host stars (which are the critical processes to produce attributes similar to ‘Oumuamua).

Kepler²³ and microlensing²⁴ surveys unveiled the omnipresence of multiple close-in super-Earths and distant sub-Neptunes around low-mass stars. These planets provide a second class of plausible parent-body candidates. Since a planet’s mass $M_p \gg M_{\text{ej}}$, a few percent efficiency per star is adequate to account for the asteroidal ISOs’ occurrence rate. In multiple systems, their eccentricity can be elevated to unity by their own dynamical instability^{25,26}. Our simulations of the tidal disruption of a self-gravity-dominated super-Earth (with $R_p = 2 \times 10^7$ m and $M_p = 11M_{\oplus}$) on an $e_0 = 0.999$ and $d_p = 4 \times 10^8$ m orbit around a $0.5M_{\odot}$ host star show that half of the fragments, with mass up to $M_{\text{upper}} \sim 0.1M_p$, can obtain a normalised orbital-energy-per-mass increment $f_E > 1$ and escape from the host star (see Methods). Through extremely close encounters with $d_p \ll d_{\text{limit}}$, super-Earths can be reduced to fragments with $M_{\text{upper}} \ll M_p$. Tidal downsizing continues until the fragments are small enough to be dominated by material strength without further disintegration (see Methods). Since for the host stars $R_s \propto M_s$ and $d_{\text{limit}}/R_s \propto M_s^{-2/3}$, tidal fragments with $a \sim 100$ m are produced more readily in the proximity of low-mass main-sequence stars. These hosts are also the most common and long-lasting stars with ubiquitous multiple super-Earths²⁷. A modest planet/star mass ratio is favourable for the planets to acquire large e_0 through dynamical instability and secular chaos²⁸, and for their fragments to be ejected. During the cooling and solidification of tidally disrupted fragments of planets’ molten cores, sintering surfaces provide adequate material strength to produce the observed c/a ratio. However, the impact of their thermal evolution on the retention of volatiles to account for ‘Oumuamua’s non-gravitational accelerations is highly uncertain (see Methods).

Similar physical processes around white dwarfs offer a third pathway for the prolific production of tidal debris^{15,29}, with a fraction of which may have rocky surfaces and sizes similar to

‘Oumuamua. As the post-main-sequence byproducts of stars, white dwarfs may retain some residual icy planetesimals and planets after their progenitors have lost their red-giant envelopes³⁰. The total population of their progenitors is largely outnumbered by that of main-sequence stars with $M_s \lesssim 0.5M_\odot$. They may contribute a small fraction of the original hosts of asteroidal ISOs (see Methods).

In our attempt to address plausible causes of all aspects of the ‘Oumuamua conundrum, we highlight the prolificacy and robustness of asteroidal ISO diffusion between stars near and far. Since these sojourns pass through the domains of habitable zones, the prospect of panspermia, carried by them (nicknamed *sola lapis*¹¹), cannot be ruled out.

1. Bannister, M. T. et al. The natural history of ‘Oumuamua. *Nature Astron.* **3**, 594–602 (2019).
2. Meech, K. J. et al. A brief visit from a red and extremely elongated interstellar asteroid. *Nature* **552**, 378–381 (2017).
3. Knight, M. M. et al. On the rotation period and shape of the hyperbolic asteroid 1I/‘Oumuamua (2017 U1) from its lightcurve. *Astrophys. J.* **851**, L31 (2017).
4. Bolin, B. T. et al. Apo time-resolved color photometry of highly elongated interstellar object 1I/‘Oumuamua. *Astrophys. J.* **852**, L2 (2017).
5. Fraser, W. C. et al. The tumbling rotational state of 1I/‘Oumuamua. *Nature Astron.* **2**, 383–386 (2018).
6. Drahus, M. et al. Tumbling motion of 1I/‘Oumuamua and its implications for the body’s distant past. *Nature Astron.* **2**, 407–412 (2018).
7. Micheli, M. et al. Non-gravitational acceleration in the trajectory of 1I/2017 U1 (‘Oumuamua). *Nature* **559**, 223–226 (2018).
8. Trilling, D. E. et al. Spitzer observations of interstellar object 1I/‘Oumuamua. *Astron. J.* **156**, 261 (2018).
9. Jewitt, D. et al. Interstellar interloper 1I/2017 U1: observations from the NOT and WIYN telescopes. *Astrophys. J.* **850**, L36 (2017).

10. Do, A., Tucker, M. A. & Tonry, J. Interstellar interlopers: number density and origin of ‘Oumuamua-like objects. *Astrophys. J.* **855**, L10 (2018).
11. Portegies Zwart, S., Torres, S., Pelupessy, I., Bédorf, J. & Cai, M. X. The origin of interstellar asteroidal objects like 1I/2017 U1 ‘Oumuamua. *Mon. Not. R. Astron. Soc.* **479**, L17–L22 (2018).
12. Engelhardt, T. et al. An observational upper limit on the interstellar number density of asteroids and comets. *Astron. J.* **153**, 133 (2017).
13. Weissman, P. R. & Levison, H. F. Origin and evolution of the unusual object 1996 PW: asteroids from the Oort cloud? *Astrophys. J.* **488**, L133–L136 (1997).
14. Čuk, M. 1I/‘Oumuamua as a tidal disruption fragment from a binary star system. *Astrophys. J.* **852**, L15 (2018).
15. Raymond, S. N., Armitage, P. J. & Veras, D. Interstellar object ‘Oumuamua as an extinct fragment of an ejected cometary planetesimal. *Astrophys. J.* **856**, L7(2018).
16. Richardson, D. C., Leinhardt, Z. M., Melosh, H. J., Bottke, W. F. & Asphaug, E. in *Asteroids III* (eds Bottke, W. F. et al.) 501–515 (Univ. of Arizona Press, Tucson, 2002).
17. McNeill, A., Trilling, D. E. & Mommert, M. Constraints on the density and internal strength of 1I/‘Oumuamua. *Astrophys. J.* **857**, L1 (2018).
18. Sridhar, S. & Tremaine, S. Tidal disruption of viscous bodies. *Icarus* **95**, 86–99 (1992).
19. Drell, S. D., Foley, H. M. & Ruderman, M. A. Drag and propulsion of large satellites in the ionosphere: an Alfvén propulsion engine in space. *J. Geophys. Res.* **70**, 3131–3145 (1965).
20. Fitzsimmons, A. et al. Spectroscopy and thermal modelling of the first interstellar object 1I/2017 U1 ‘Oumuamua. *Nature Astron.* **2**, 133–137 (2018).
21. Kaib, N. A. & Quinn, T. Reassessing the source of long-period comets. *Science* **325**, 1234–1236 (2009).
22. Punzo, D., Capuzzo-Dolcetta, R. & Portegies Zwart, S. The secular evolution of the Kuiper belt after a close stellar encounter. *Mon. Not. R. Astron. Soc.* **444**, 2808–2819 (2014).

23. Coughlin, J. L. et al. Planetary candidates observed by Kepler. VII. The first fully uniform catalog based on the entire 48-month data set (Q1-Q17 DR24). *Astrophys. J. Suppl. Ser.* **224**, 12 (2016).
24. Cassan, A. et al. One or more bound planets per milky way star from microlensing observations. *Nature* **481**, 167–169 (2012).
25. Nagasawa, M., Ida, S. & Bessho, T. Formation of hot planets by a combination of planet scattering, tidal circularization, and the Kozai mechanism. *Astrophys. J.* **678**, 498–508 (2008).
26. Ida, S., Lin, D. N. C. & Nagasawa, M. Toward a deterministic model of planetary formation. VII. Eccentricity distribution of gas giants. *Astrophys. J.* **775**, 42 (2013).
27. Charbonneau, D. et al. A super-Earth transiting a nearby low-mass star. *Nature* **462**, 891–894 (2009).
28. Davies, M. B. et al. in *Protostars and Planets VI* (eds Beuther, H. et al.) 787–809 (Univ. of Arizona Press, Tucson, 2014).
29. Rafikov, R. R. 11/2017 ‘Oumuamua-like interstellar asteroids as possible messengers from dead stars. *Astrophys. J.* **861**, 35 (2018).
30. Veras, D., Wyatt, M. C., Mustill, A. J., Bonsor, A. & Eldridge, J. J. The great escape: how exoplanets and smaller bodies desert dying stars. *Mon. Not. R. Astron. Soc.* **417**, 2104–2123 (2011).

Correspondence and requests for materials Correspondence and requests for materials should be addressed to Y.Z.

Acknowledgements Y. Z. acknowledges funding from the Université Côte d’Azur “Individual grants for young researchers” program of IDEX JEDI. D.N.C.L. thanks Institute for Advanced Studies, Princeton for support while this work was initiated. We thank Scott Tremaine for inspiration and suggestions, Derek C. Richardson for assistance with the PKDGRAV code, Gregory Laughlin, Patrick Michel, Shangfei Liu, Roman Rafikov, and Simon Portegies Zwart for constructive feedback on the results and implications of this work. Simulations were carried out at the University of Maryland on the yorp cluster administered by

the Department of Astronomy and the deepthought and deepthought2 supercomputing clusters administered by the Division of Informational Technology. For data visualisation, the authors made use of the freeware, multiplatform, ray-tracing package, Persistence of Vision Raytracer.

Author contributions Y.Z. performed the soft-sphere/ N -body numerical simulations, the thermal modelling, and analysed the numerical results and implications for ‘Oumuamua. D.N.C.L. initiated the collaboration to study tidal disruption as a formation mechanism for ‘Oumuamua, and contributed to address questions on ISOs’ population and dynamical origins. Both authors contributed to interpretation of ‘Oumuamua’s properties and preparation of the manuscript.

Author information *National Astronomical Observatory of China, Beijing, China* Yun Zhang

Institute for Advanced Studies, Tsinghua University, Beijing, China Yun Zhang & Douglas N. C. Lin

Université Côte d’Azur, Observatoire de la Côte d’Azur, CNRS, Laboratoire Lagrange, Nice, France Yun Zhang

Department of Astronomy, University of Maryland, College Park, MD, USA Yun Zhang

Department of Astronomy and Astrophysics, University of California, Santa Cruz, CA, USA Douglas N. C. Lin

Competing interests The authors declare no competing interests.

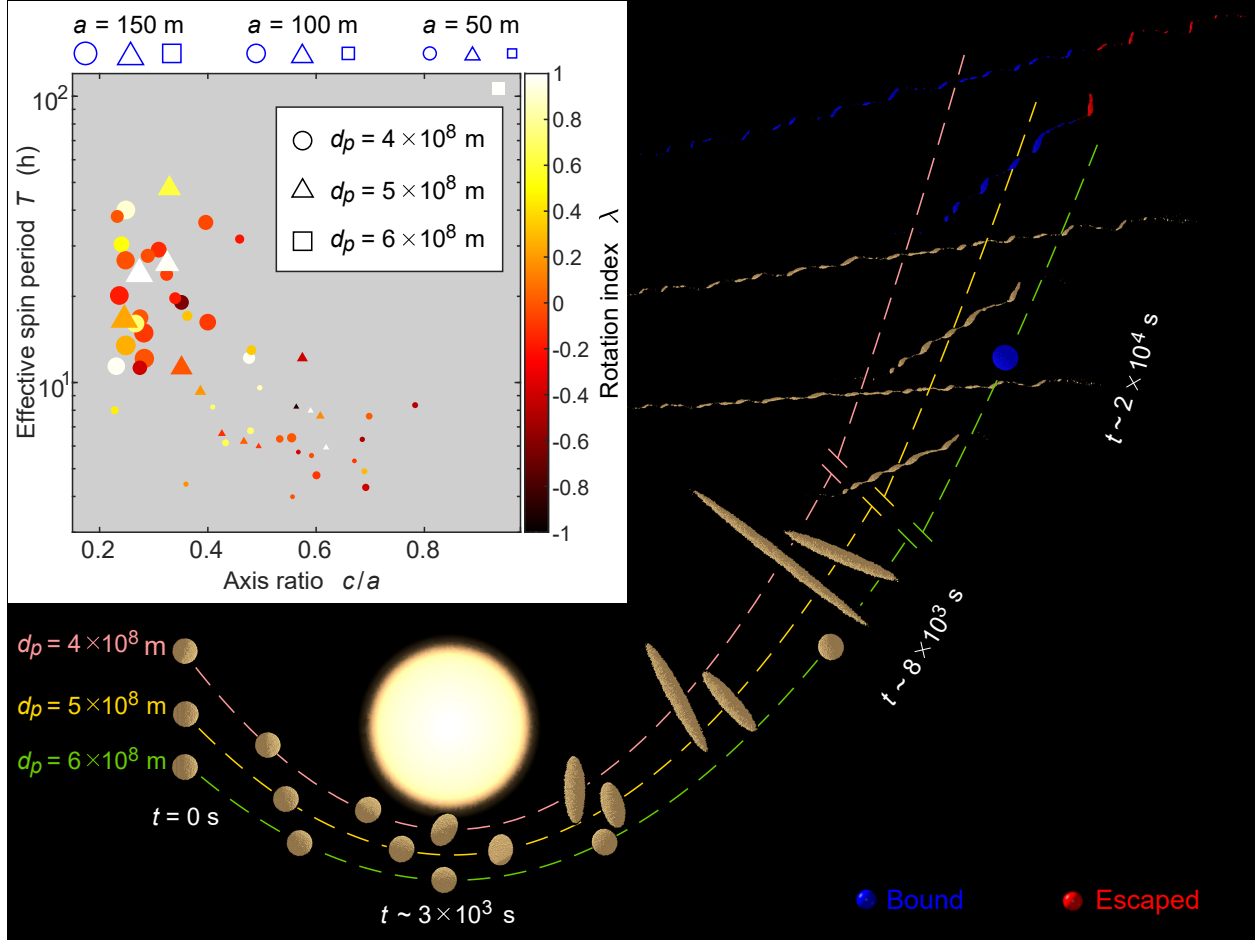


Figure 1: **Tidal disruption processes and fragmentation outcomes at different periastron distances for the first set of models.** The main panel superimposes the trajectories (the dashed lines) and the evolution of the rubble-pile parent body (the beige granular aggregates with mass centres locating at each corresponding trajectory; enlarged for illustration purpose) at different times t as it flies by the star (from left to right), with three pericentre separations d_p . The luminous sphere represents the position and size of the star. The resulting fragments at the last scene are coloured by their orbit types, where the red ones can escape from their original planetary system and become interstellar objects. The top-left inset shows the distributions of the effective spin period T and the short-to-long axis ratio c/a of resulting fragments with mass $\geq 10^6$ kg. The symbol size represents the semi-major axis a for each fragment, and colour denotes the rotation index, where $\lambda = 1, 0$, and -1 indicate the short-, intermediate-, and long-axis rotation states, respectively, and values in between indicate non-principal-axis rotation states (see Methods). A friction angle of 35° and a cohesive strength of 0 Pa are used in these simulations.

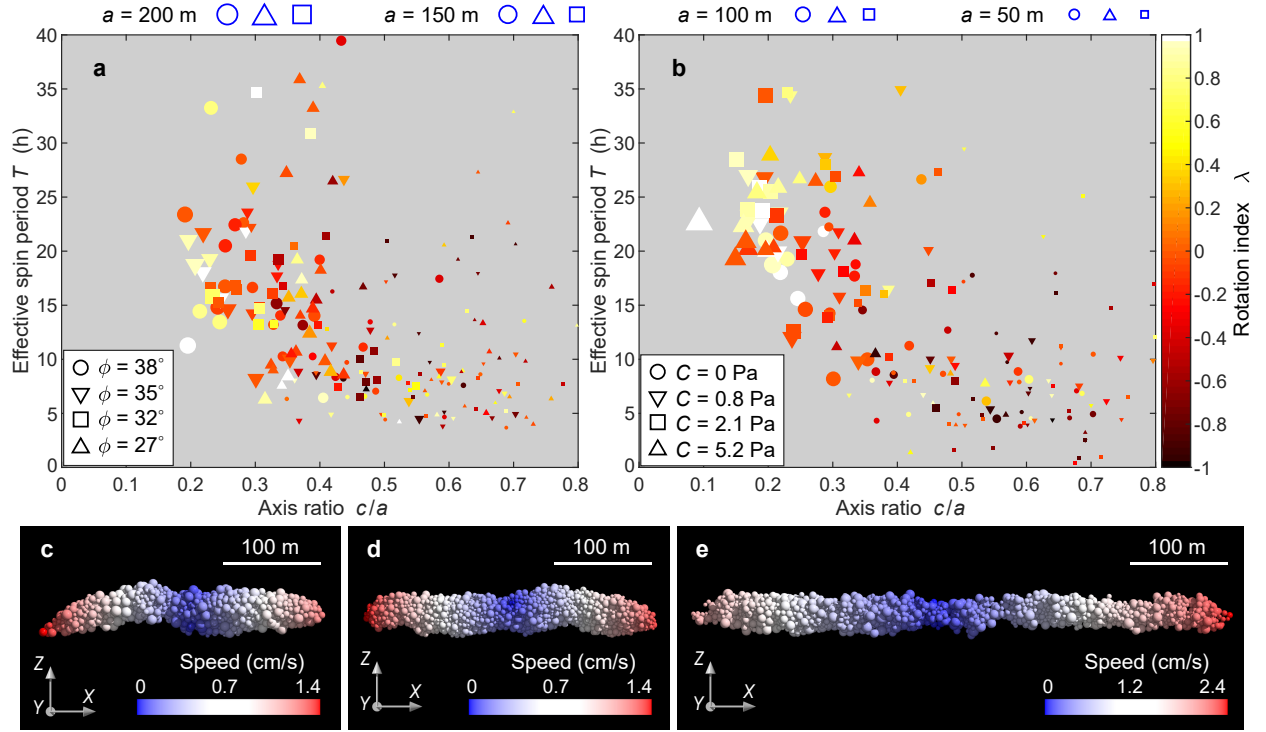


Figure 2: **Fragmentation outcomes of a range of material strengths at $d_p = 3.5 \times 10^8$ m for the first set of models.** **a, b**, Effective spin period and axis ratio distributions of fragments with mass $\geq 10^6$ kg for different material friction angles ϕ (**a**; $C = 0$ Pa) and different later-turned-on material cohesive strengths C (**b**; $\phi = 35^\circ$). The symbols have the same meanings as in the top-left inset of Fig. 1. **c, d, e**, Examples of elongated fragments formed by tidal disruption (**c, d**, $\phi = 35^\circ$, $C = 0$ Pa; **e**, $\phi = 35^\circ$, $C = 0$ Pa before crust formation at 3 hours post periastron and $C = 5.2$ Pa after this transition), where the colours show the bulk rotation.

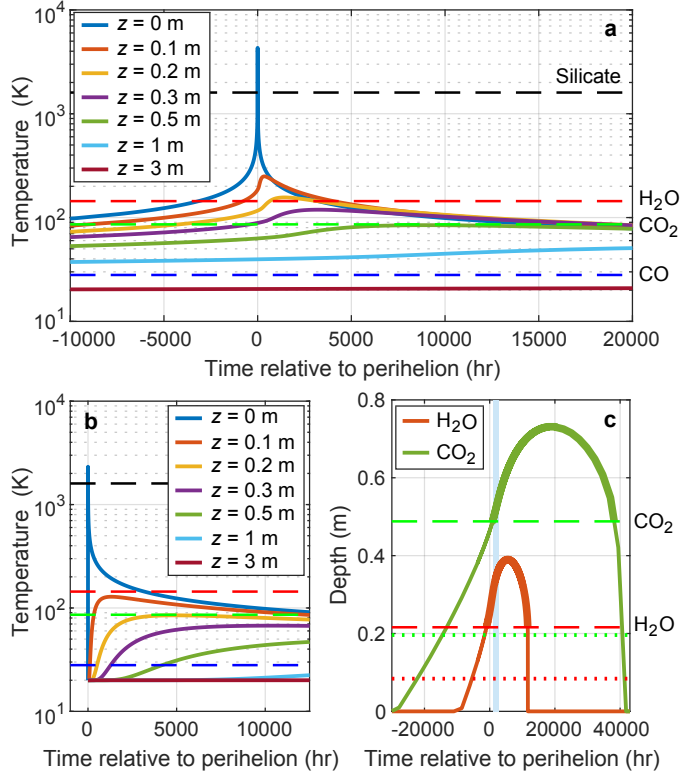


Figure 3: **Thermal modelling of a close stellar flyby.** **a**, Temperature evolution of the parent body during its tidal encounter with the host star ($M_s = 0.5M_\odot$) on a parabolic orbit with a periastron distance $d_p = 3.5 \times 10^8$ m. **b**, Temperature evolution of a fragment with an initial temperature of 20 K, whose surface is freshly exposed to the star after the parent body is broken up during the periastron passage on the same orbit. In **a** and **b**, the temperature at various depths is represented by solid lines with different colours, and the vacuum sublimation temperatures³¹ for H₂O, CO₂, and CO, and the melting temperature of silicate³² are represented by dashed lines. **c**, depth evolution of the H₂O and CO₂ sublimation layers during 'Oumuamua's flyby of the Sun. The red and green dashed/dotted lines represent the buried depths of residual H₂O and CO₂ ices in the formation scenario shown in **a/b**. The observation span of 'Oumuamua is indicated by the light-blue region. Plenty of residual H₂O and CO₂ ices can commence sublimation during the Solar System passage as indicated by the bold lines.

Methods

Soft-sphere discrete element model. We model the parent body as a self-gravitational aggregate consisting of $\sim 20,000$ spheres with a -3 -index power-law particle size distribution (i.e., $d \ln N / d \ln S = -3$, where N is the number of particles and S is the particle size). Within the high-efficiency parallel tree code framework, PKDGRAV^{33,34}, a soft-sphere contact model is used for computing particle contact forces with four components in the normal, tangential, rolling, and twisting directions³⁵⁻³⁷. The compressive strength of the material is controlled by two stiffness constants, (k_N, k_S) , for the normal and tangential directions; the contact energy dissipation is controlled by two coefficients of restitution, $(\varepsilon_N, \varepsilon_S)$, for the normal and tangential directions; the material shear strength is controlled by three friction coefficients for the tangential, rolling, and twisting directions, (μ_S, μ_R, μ_T) , and a shape parameter, β ; and the material cohesive strength is controlled by an interparticle cohesive tensile strength, c_p , along the normal direction.

The contact model as well as the relation between parameter setup and material strengths have been calibrated with laboratory experiments on real sands^{35,37}. To precisely integrate the interactions between particles, the timestep Δt is set to 0.01 s for the simulations considered here. The normal stiffness k_N is set to ensure that particle overlaps do not exceed 1% of the minimum particle radius. The tangential stiffness k_S is set to $(2/7)k_N$ to keep normal and tangential oscillation frequencies equal to each other. The coefficients of restitution, ε_N and ε_S , are set to 0.55 resembling the energy dissipation behaviours of terrestrial rocks³⁸. μ_R and μ_T are set to 1.05 and 1.3, respectively, corresponding to sand particles of medium hardness³⁹. The free parameters μ_S and β are used to adjust the material friction angle³⁶ ϕ , for which $\mu_S = 0.2$ and $\beta = 0.3$ corresponds to a friction angle of 27° , $\mu_S = 0.5$ and $\beta = 0.4$ corresponds to a friction angle of 32° , $\mu_S = 1.0$ and $\beta = 0.5$ corresponds to a friction angle of 35° , and $\mu_S = 1.3$ and $\beta = 0.7$ corresponds to a friction angle of 38° . The interparticle cohesion c_p is used³⁷ to adjust the material cohesive strength C , for which $c_p = 100$ Pa corresponds to $C = 0.8$ Pa, $c_p = 200$ Pa corresponds to $C = 2.1$ Pa, and $c_p = 400$ Pa corresponds to $C = 5.2$ Pa for a constant friction angle of 35° .

Fig. 2a shows more elongated fragments are formed with a larger friction angle. This dependence is expected because higher shear resistance can slow down the relative motion between the constituent particles as well as maintain the stability of more extreme shape. Normally, the

friction angle of granular material is in the range of 25° to 45° . Our numerical experiments show that extremely elongated fragments with axis ratios of ~ 0.3 can form even for a material friction angle as low as 27° . This implies that production of elongated fragments through tidal disruption is robust. Nevertheless, the particles' relative motion is hard to be damped out completely by friction alone and $c/a < 0.2$ is hard to achieve even using a friction angle above 40° . The inclusion of initial, constant cohesion into the parent body's material also cannot help to form a more elongated fragment (see Supplementary Fig. 2 and Supplementary Video 2).

However, the material cohesive strength of the parent body and its fragments can be changed by the thermal effect during their periastron passage. In proximity of their original host, their exposed surfaces could be briefly heated by the intense stellar radiation to a temperature above the melting point of silicates, i.e., $T \geq 1600$ K (see Fig. 3). On their outward journey, the solidification of their surfaces facilitates the formation of sintering bonds between surface particles^{40,41}. The enhanced cohesive strength inhibits subsequent break-apart and enables the formation and survival of some very elongated fragments. We carried out a series of phase-transition simulations in which cohesion between particles in the parent body is imposed 3 hours after the periastron passage (when the silicates can re-condense). The production of fragments with $c/a \lesssim 0.1$ under such a circumstance is shown in Fig. 2b and Supplementary Video 3.

We also explored the effects of shape, initial rotation state, and particle size distribution and resolution of the parent body in the tidal disruption simulations (see Supplementary Figs. 3–5). The production of elongated fragments with $c/a < 0.3$ is robust in all the simulations.

Tidal disruption limiting distance. When an object approaches a star within the Roche limit, tidal forces imposed by the star overwhelm the gravitational forces that hold the object together and may disrupt it. The Roche limit of an initially spherical, non-spinning, viscous fluid object is¹⁸

$$d_{\text{Roche}} = 1.05 \left(\frac{M_s}{\rho_p} \right)^{1/3},$$

where ρ_p is the bulk density of the object and M_s is the mass of the star. d_{Roche} is appropriate to predict the tidal disruption limiting distance for bodies in the gravity-dominated regime, such as gas giants, super-Earths with molten interiors, minor and dwarf planets.

While for small bodies in the material-strength-dominated regime, their intrinsic material

shear and cohesive strengths can prevent tidal disruption within this limit. To reflect the material characteristics, we use the elastic-plastic continuum theory⁴² to estimate the tidal disruption limit of small bodies in the material-strength-dominated regime,

$$d_{\text{str}} = \left(\frac{\sqrt{3}}{4\pi}\right)^{1/3} \left(\frac{5C}{4\pi G R_p^2 \rho_p^2} + \frac{2 \sin \phi}{\sqrt{3}(3 - \sin \phi)}\right)^{-1/3} \left(\frac{M_s}{\rho_p}\right)^{1/3},$$

which depends on the radius of the object R_p , and decreases with either a larger friction angle ϕ or a stronger cohesive strength C . G is the gravitational constant. This limit is much smaller than the Roche limit, e.g., even for low-strength materials with $\phi = 25^\circ$ and $C = 0$ Pa, $d_{\text{str}} = 0.9(M_s/\rho_p)^{1/3} < d_{\text{Roche}}$. Material strength in small bodies provides a stabilising effect against the host star's tidal perturbations.

When the object's cohesive strength $C > 0$ Pa, d_{str} is size-dependent. For example, during a close flyby with a star with $M_s = 0.5M_\odot$ and $R_s = 0.5R_\odot \sim 3.5 \times 10^8$ m, a cohesionless object with $\rho_p = 2,000$ kg m⁻³ and $\phi = 35^\circ$ can be tidally distorted if the periastron distance $d_p \leq d_{\text{str}} = 6.3 \times 10^8$ m. If its material contains a cohesive strength $C = 5.2$ Pa, and its radius $R_p = 100$ m, d_{str} would be decreased to 4×10^8 m. For a 10-m-radius object with equivalent material strengths, $d_{\text{str}} \simeq 9.5 \times 10^7$ m $< R_s$, indicating that smaller bodies are much harder to be tidally disrupted outside the stellar surface. It also indicates that 100-m-sized fragments with some cohesion can be preserved without further fragmentation outside R_s . These analyses are consistent with our simulation results, which show that an 100-m-radius object with equivalent properties and no cohesion is slightly distorted when passing by the star at a distance of 6×10^8 m (see Fig. 1) whereas it can preserve its integrity with $C = 5.2$ Pa at a smaller d_p ($\sim 4 \times 10^8$ m).

As the transition between regimes occurs at a few km radius, the limiting distance for tidal disruption is given by d_{Roche} in the gravity-dominated regime and d_{str} in the material-strength-dominated regime as

$$d_{\text{limit}}(R_p) = \begin{cases} d_{\text{Roche}}, & R_p \gtrsim 1 \text{ km}; \\ d_{\text{str}}, & R_p \lesssim 1 \text{ km}. \end{cases}$$

Since $d_{\text{limit}} \propto (M_s/\rho_p)^{1/3}$, our simulation results can be scaled to different stellar mass M_s and parent-body bulk density ρ_p .

As $R_s \propto M_s$ for main-sequence stars, $d_{\text{limit}}/R_s \propto M_s^{-2/3}$, the region where tidal disruption occurs, i.e., $R_s < d_p \lesssim d_{\text{limit}}$, is much larger around lower-mass stars. For most of the Solar System bodies, $d_{\text{limit}} \lesssim R_\odot$, in which case they would crush into the Sun's surface before tidal fragmentation. Some solar twin binary stars with planets exhibit signs of super-Earth ingestion⁴³. This fragmentation barrier also accounts for the absence of small bodies in the Solar System with an extreme shape like 'Oumuamua. In contrast, $d_{\text{limit}}(R_p \gtrsim 1 \text{ km})$ is much larger than R_s for stars with $M_s < 0.8M_\odot$. For a moderate cohesive strength $C = 10 \text{ Pa}$, which can be readily provided by the sintering bonds formed during close stellar encounters, the radii of low-mass stars are comparable to $d_{\text{limit}}(R_p \sim 10\text{--}100 \text{ m})$. Therefore, planets and planetesimals around low-mass stars can be efficiently tidal-downsized to sub-km-sized fragments.

Most recently emerged white dwarfs in globular star clusters⁴⁴ have $M_s \geq 0.53M_\odot$ and $R_s \sim 10^{-2}R_\odot$. Older isolated white dwarfs have comparable R_s and M_s . Since their $d_{\text{limit}} \gg R_s$, there is a vast range of d_p for tidal downsizing of planets and residual planetesimals. For a moderate cohesive strength $C = 10 \text{ Pa}$, this downsizing can powderise these bodies into centimetre-sized fragments at a periastron distance $d_p \sim R_s$. The production and preservation of 'Oumuamua-size ISOs (with $a \sim 100 \text{ m}$) requires the parent body passing the host at a distance of $d_p \sim d_{\text{limit}}(100 \text{ m}) \sim 0.5R_\odot$.

Ejection condition. As a single entity, the parent body passes through its periastron with an orbital speed $V_p = \sqrt{(1 + e_0)GM_s/d_p}$ in the direction $\hat{\mathbf{V}}_p$, a unit orbital angular velocity vector $\hat{\mathbf{\Omega}} = \hat{\mathbf{d}}_p \times \hat{\mathbf{V}}_p$ and total energy per unit mass

$$E_0 = -\frac{GM_s(1 - e_0)}{2d_p}.$$

Under the intense tidal torque, the parent body acquires a prograde uniform spin angular frequency $\Omega_f = fV_p/d_p$, where f is a factor of order unity. After its tidal disruption, the fragments at distance r_f from the parent body's centre of mass (in the direction $\hat{\mathbf{r}}_f$) acquire a modified velocity (relative to the host star)

$$\mathbf{V}'_p = \mathbf{V}_p + \Omega_f r_f \hat{\mathbf{\Omega}} \times \hat{\mathbf{r}}_f.$$

For simplicity, we consider those fragments at $r_f = \pm R_p/2$ (i.e., half of the parent body's size on the far and near side to the host star, relative to the parent body's centre of mass) and set $\hat{\mathbf{r}}_f = \hat{\mathbf{d}}_p$.

Since the individual fragments are no longer bound to each other, their energy per unit mass is modified to

$$E'_{\pm} = -\frac{GM_s}{d_p \pm R_p/2} + \frac{(V_p \pm \Omega_f R_p/2)^2}{2} \simeq -\frac{GM_s(1 - e_0)}{2d_p} \pm \frac{GM_s(1 + 2f)R_p}{2d_p d_p}.$$

After the tidal disruption of the parent body, the fractional incremental energy change

$$|f_E| = \frac{|E'_{\pm} - E_0|}{|E_0|} \simeq \frac{(1 + 2f) R_p}{(1 - e_0) d_p}$$

of the fragments in its outer region (with $r_f > R_p/2$) exceeds unity for

$$1 - e_0 \lesssim 1 - e_{0,\text{crit}} = (1 + 2f) \frac{R_p}{d_p}.$$

In this limit, up to half of the fragments acquire sufficient energy to escape from the gravitational confinement of the host star. Since $(1 - e_{0,\text{crit}}) \propto R_p$, this ejection criterion is more stringent for small-size parent bodies.

Around host stars that bear planets (with mass M_J and orbital semi-major axes a_J), additional gravitational binding energy $\Delta E = -GM_J/d$ needs to be taken into account at distance $d > a_J$. Since the post-periastron energy E' is conserved at $d < a_J$, the criterion for fragments to escape is $E' > \Delta E$ or equivalently,

$$1 - e_0 \lesssim \frac{(1 + 2f) R_p}{(1 + 2M_J a_0 / M_s a_J) d_p}.$$

The modification due to the Jovian-mass planet is generally small unless the initial $a_0 \gg a_J$. Parent bodies would be retained in the regions beyond the planets (analogous to the Kuiper belt and the Oort cloud in the Solar System), if their

$$R_p \lesssim \frac{2}{(1 + 2f)} \frac{M_J d_p^2}{M_s a_J}.$$

Rotation state. The rotation state of a body can be characterised by the effective spin period T and the dynamic inertia I_D , which are the spin period and moment of inertia of a sphere with an equivalent total rotational energy and momentum, respectively⁴⁵. The rotation mode of the body can be inferred from the value of I_D . With principal moments of inertia $I_z > I_y > I_x$, the body rotates along its maximum moment of inertia if $I_D = I_z$; the body's spin axis precesses along its

maximum moment of inertia (i.e., short-axis mode, SAM) if $I_z > I_D > I_y$; the body rotates along its intermediate moment of inertia if $I_D = I_y$; the body’s spin axis precesses along its minimum moment of inertia (i.e., long-axis mode, LAM) if $I_y > I_D > I_x$; and the body rotates along its minimum moment of inertia if $I_D = I_x$. Accordingly, we define the rotation index λ as

$$\lambda = \begin{cases} (I_D - I_y)/(I_z - I_y), & I_D \geq I_y; \\ (I_D - I_y)/(I_y - I_x), & \text{otherwise.} \end{cases}$$

Therefore, $\lambda = 1, 0, -1$ indicates the principal-axis rotation state about the maximum, intermediate, and minimum moment of inertia, respectively. $0 < \lambda < 1$ indicates SAM and $-1 < \lambda < 0$ indicates LAM.

Our simulations show that the fragments of tidal disruption primarily have prolate triaxial shape (see Figs. 1, 2, and Supplementary Fig. 1). Although brightness variations of ‘Oumuamua indicate an extremely small short-to-long axis ratio, the shape of this object is poorly constrained due to lack of knowledge about its rotation state and albedo variation⁴⁶. The most comprehensive model published to date⁴⁷ found that the large-amplitude variation in ‘Oumuamua’s light curve can be interpreted as a tumbling prolate object with an axis ratio of $c/a \sim 1/8$ or a tumbling oblate object with an axis ratio of $c/a \sim 1/6$. The probabilities of reproducing light curve minima as deep as the observed values with a randomly oriented angular momentum vector are 16% for the best-fit 1/8 prolate and 91% for the 1/6 oblate model. Since the value of the axis ratio depends on the orientation of the rotation pole, a more comprehensive probability comparison is warranted for a range of prolate and oblate triaxial models (in addition to the best-fit models).

Among all of the small bodies in the Solar System with high-quality shape data⁴⁸, none of the oblate objects have an axis ratio $c/a \leq 0.4$ while some prolate ones have an axis ratio $c/a \sim 0.2$. This distribution implies an extremely elongated “cigar-like” shape is more likely than an extremely flat “pancake-like” shape. The prolate shape is also energetically more stable and permits a much larger range of orientations of rotation pole on the sky⁴⁶.

Damping timescales. The stress-strain cycling caused by the non-principal-axis rotation within a non-rigid body will ultimately bring the axis of rotation into alignment with its principal axis of the maximum moment of inertia. The characteristic damping timescale of the tumbling rotation

can be estimated by⁴⁹

$$\tau_d \simeq \frac{P^3}{C_d^3 D^2},$$

where P and D are the rotation period and mean diameter of the body, respectively, and C_d is a constant related to the rigidity, energy dissipation property and shape of the body. For P measured in hours, D measured in kilometres, and τ_d measured in Gyr (10^9 years), the value of C_d is about 17 ± 2.5 . For a hundred-meter-sized fragment formed by tidal disruption, the rotation period P usually ranges from ~ 5 hours to ~ 50 hours (see Fig. 2) and the mean diameter $D \simeq 2\sqrt[3]{abc} \simeq 60$ m, predicting $5 \times 10^9 \leq \tau_d \leq 1 \times 10^{13}$ years, consistent with the damping timescales estimated for ‘Oumuamua⁵.

Thermal modelling. To evaluate the temperature evolution of an object during close encounters with its original main-sequence host star, we use a finite-difference numerical technique to model the heat conduction process. For comparison with previous analyses for ‘Oumuamua²⁰, the same setup is applied for the thermal modelling, in which the object has a comet-like Bond albedo of 0.01, a bolometric emissivity of 0.95, a thermal conductivity of $0.001 \text{ W m}^{-1} \text{ K}^{-1}$, a bulk density of $1,000 \text{ kg m}^{-3}$, and a heat capacity of $550 \text{ J kg}^{-1} \text{ K}^{-1}$. Assuming an encounter with a star with a mass of $0.5M_\odot$, the stellar flux at 1 AU is about $(0.5)^{3.5} F_\odot(1 \text{ AU}) \simeq 121 \text{ W m}^{-2}$, where F_\odot is the local integrated flux of the Sun. The thermal modelling results can be scaled to different thermal property values²⁰. To show that volatiles in the subsurface can be preserved even under the most extreme condition, we intentionally looked at the most intensive illumination condition. The simulated surface element is assumed to be permanently illuminated by the star during the encounter, and an orbit with a small periastron distance $d_p = 3.5 \times 10^8 \text{ m}$ is used for the thermal analyses.

The simulation was started 153,000 days before periastron when the object was over 250 AU away from the star, where it had a temperature close to the interstellar temperature $\sim 10 \text{ K}$. As shown in Fig. 3a, the surface temperature significantly increases 200 days before periastron, but the subsurface region is almost impervious to the heat of the star. H_2O ice buried $\gtrsim 0.2 \text{ m}$ and CO_2 ice buried $\gtrsim 0.5 \text{ m}$ beneath the surface can be preserved. The thermal simulation tracked the temperature evolution until 110,000 days after periastron (well beyond the range showed in Fig. 3). The results show that the slow inward propagation of periastron heat can activate the sublimation

of CO ice buried below a depth of 3 m which is a large fraction of ‘Oumuamua’s minor axis c . The thorough clearing of low-sublimation-temperature volatiles accounts for the lack of visible cometary activities around ‘Oumuamua during its subsequent perihelion passage through the Solar System in 2017.

If ‘Oumuamua is one of the fragments that originated from the parent body’s undifferentiated interior, most of its surface area would be exposed to the star only after the periastron passage. Less heat would be transferred to the interior (see Fig. 3b) and more volatiles could be preserved at a shallower depth in its interior (H₂O ice buried $\gtrsim 0.1$ m and CO₂ ice buried $\gtrsim 0.2$ m beneath the surface can be preserved).

Similar models can be constructed for main-sequence stars with different mass. The flux near the stellar surface is $\propto M_s^{1.5}$ (because the luminosity is $\propto M_s^{3.5}$ and $R_s \propto M_s$). Grazing passage in the proximity of the stellar surface (over a timescale $\propto M_s$) can heat the surfaces of intruding objects well above the sublimation temperature of the volatile ices. However, the sub-surface volatile deposits may be less efficiently depleted during the brief encounters with less luminous low-mass stars. Around main-sequence hosts, energy dissipation due to the internal friction between particles is too weak to cause a significant amount of volatile losses.

We also consider the possibility of white dwarfs as ‘Oumuamua’s original host stars. Prior to their emergence, their progenitors go through a red giant phase when their envelopes engulf planets and asteroids within a few AU and their radiation increases the equilibrium temperature within ~ 100 AU above most volatiles’ sublimation temperature. During their subsequent mass loss to surrounding planetary nebula, a fraction of their outer planets and residual planetesimals remain attached, though with more expanded orbits, to the white dwarfs’ gravity⁵⁰. They join the reservoir of potential parent bodies of asteroidal ISOs (see section ‘‘Asteroidal ISOs’ mass budget’’ in Methods).

After the planetary nebula is dispersed, the luminosity of white dwarfs decreases from hundredths of the luminosity in their main-sequence stage at age $\lesssim 0.1$ Gyr to ten thousandth of that after 10 Gyr. For these ages, the equilibrium temperatures at $d_{\text{limit}}(R_p = 100 \text{ m}) \sim 0.5R_\odot$ are 2600 K and 820 K for a $0.5M_\odot$ white dwarf, respectively, well above the sublimation temperatures of volatiles. The fragments’ silicate surfaces may become molten and their cohesive strength may

be enhanced by the subsequent solidification. For grazing encounters with $d_p \sim R_s$, although smaller ($R_p \gtrsim 0.1$ m) objects can withstand the intense tidal stress, they are expected to be totally sublimated with 7 times higher equilibrium temperatures and accreted onto the white dwarfs in a gas phase⁵¹.

During ‘Oumuamua’s recent excursion in the Solar System, its surface was once again exposed by the Sun’s intense radiation. Heat diffusion can activate the sublimation of residual H₂O and CO₂ ices^{7,52}. We simulated the heat conduction process for ‘Oumuamua during its Solar System passage using the same thermal properties introduced in the first paragraph of this section. The simulation was started 51,000 days before perihelion when ‘Oumuamua was over 780 AU away from the Sun and had a initial temperature of 10 K. The thermal analyses indicate that, during the span of observation, the sublimation temperature of H₂O ices is reached at ~ 0.4 m beneath the surface, and that of CO₂ is reached at ~ 0.5 m (see Fig. 3c), consistent with previous results^{7,20}. Due to the consumption of H₂O and CO₂ during our hypothetical formation process, the CO₂ buried in subsurface may not be activated during the observation, while the volatile inventory of H₂O is sufficient to provide the observed non-gravitational acceleration (see section “Vaporising H₂O ice by solar irradiation to provide the non-gravitational acceleration” in Methods). Because of the time delay involved in thermal processes, the outgassing of H₂O in the subsurface should commence several days later after reaching sublimation temperature. This outgassing activity is consistent with the low CO₂ production rate during the observation⁸ and the non detection of H₂O during ‘Oumuamua’s perihelion passage⁵³.

Motion relative to the Local Standard of Rest (LSR). Prior to ‘Oumuamua’s passage through the Solar System, its velocity relative to the LSR ($v_O \sim 10$ km s⁻¹) is small compared with that of mature solar type stars². Stars in the solar neighbourhood are formed in turbulent giant molecular clouds (GMCs) that also gravitationally stir stars to gain velocity dispersion relatively to the LSR⁵⁴. Their velocity dispersion relative to the LSR is observed⁵⁵ to be

$$v_d(\tau_s) \sim v_{d0}(\tau_s/\tau_{d0})^{1/2},$$

where $v_{d0} \simeq 10$ km s⁻¹, $\tau_{d0} \simeq 1$ Gyr, and τ_s is the stellar age. Relative to v_d , the modest value of v_O may imply ‘Oumuamua comes from a young stellar system, although the possibility that it has been travelling in the interstellar medium (ISM) for billions of years cannot be ruled out^{2,11}. Here

we analyse the potential effects of the ISM drag and the coupling of motion with magnetic fields on the ISOs' velocity relative to the LSR.

The energy per unit mass of ISOs' random motion increases at a rate $\dot{e}_{\text{gain}} = (1/2)dv_d^2/d\tau \sim v_{d0}^2/2\tau_{d0}$. The motion of ISOs through the ISM (with a density n_{ISM}) also leads to energy dissipation at a rate

$$\dot{e}_{\text{diss}} \sim \frac{C_D n_{\text{ISM}} m_p v_d^3 \pi a c}{\pi a c^2 \rho_O},$$

where C_D is the drag coefficient of order unity, m_p is the mass of a proton, c and a are the sizes of a prolate ellipsoid with semi-minor and semi-major axes (in the range of 10–100 m for 'Oumuamua), ρ_O is the bulk density (assuming $\sim 1,000 \text{ kg m}^{-3}$ for 'Oumuamua), and mass $M_O \sim \pi \rho_O a c^2$, respectively. They reach a terminal speed with

$$v_{\text{term}} \simeq \left(\frac{\rho_O c \dot{e}_{\text{gain}}}{C_D n_{\text{ISM}} m_p} \right)^{1/3} \sim v_{d0} \left(\frac{c}{10 \text{ m}} \frac{\rho_O}{10^3 \text{ kg m}^{-3}} \frac{10^{10} \text{ m}^{-3}}{n_{\text{ISM}}} \right)^{1/3}.$$

Among the ISM's multiple components⁵⁶, the warm ionised or neutral hydrogen gas has $n_{\text{ISM}} \sim 10^6 \text{ m}^{-3}$, which is too tenuous to make a difference. Although the GMCs have $n_{\text{ISM}} \sim 10^{10}$ – 10^{12} m^{-3} , they occupy $< 1\%$ of the volume and cannot be effective decelerators unless 'Oumuamua was trapped in them. The cold neutral gas has $n_{\text{ISM}} \lesssim 10^8 \text{ m}^{-3}$ and fills a much larger fractional volume than the GMCs, especially near the mid-galactic plane. It can only reduce v_{term} to be comparable to that of 'Oumuamua's motion^{57,58} if 'Oumuamua's $\rho_O \ll 1,000 \text{ kg m}^{-3}$.

The ISM also contains magnetic fields with $B \sim 10 \mu\text{G} = 1 \text{ nT}$ in the neutral medium and a few times larger in the molecular clouds^{56,59}. As 'Oumuamua moves through the field, an electric field $\mathbf{v} \times \mathbf{B}$ is induced across it with an electric potential $U \sim avB$. An Alfvén wave is emitted along a wing¹⁹ with a power

$$P \simeq U^2/R_{\text{wing}} = a^2 v^2 B^2 / \mu_0 v_A.$$

In SI units, $R_{\text{wing}} \sim \mu_0 v_A$ is the effective resistance⁶⁰ provided by the surrounding plasma, $\mu_0 = 4\pi \times 10^{-7} \text{ N A}^{-2}$ is the permeability of free space, and $v_A \sim 1 \text{ km s}^{-1}$ is the Alfvén speed. This power dissipates 'Oumuamua's kinetic energy per unit mass at a rate $dv^2/dt \simeq P/M_O$. When the power dissipated in the Alfvén wing is balanced by \dot{e}_{gain} , a terminal speed is established with

$$\frac{v_{\text{term}}}{v_{d0}} \simeq \left(\frac{\pi c^2 \rho_O \mu_0 v_A}{2a \tau_{d0} B^2} \right)^{1/2} \simeq 7 \left(\frac{\rho_O}{10^3 \text{ kg m}^{-3}} \right)^{1/2} \left(\frac{c}{10 \text{ m}} \right)^{1/2} \left(\frac{10c}{a} \right)^{1/2} \left(\frac{v_A}{1 \text{ km s}^{-1}} \right)^{1/2} \left(\frac{1 \text{ nT}}{B} \right)$$

in SI units. In regions with $B \sim$ a few nT, small ($c \lesssim 10 \text{ m}$) ISOs v_{term} is marginally comparable to $v_{d0} \sim 10 \text{ km s}^{-1}$ and ‘Oumuamua’s observed velocity relative to the LSR. The terminal speed for ISOs with $a \sim c \geq 1 \text{ km}$, is comparable to the dispersion speed with respect to the LSR for stars with comparable age.

In the above estimate, we have assumed the magnetic diffusion timescale $\tau_m \sim a^2/\eta$ is shorter than the tumbling timescale T_{tum} . The magnetic diffusivity η is $1/\mu_0\sigma_e$, where the electric conductivity σ_e of cold rock⁶¹ can be as low as 10^{-6} S m^{-1} . In this limit, $\tau_m \ll T_{\text{tum}}$ such that the field is decoupled from ‘Oumuamua’s tumbling motion⁶². In order to determine the drag on the ‘Oumuamua’s spin (with a frequency ω_O) by the Alfvén wave⁶³, we consider that its centre of mass is at rest with the interstellar magnetic field and its spin axis is along its minor axis and is inclined to the field lines at an angle θ . The spin of ‘Oumuamua in the field induces an effective potential drop $\sim \sin\theta B\omega_O a^2/8$ between each end and the centre of mass of the spheroid (over a length $a/2$). The total power emitted by the Alfvén waves at both ends of the spheroid is $\sim \sin^2\theta B^2\omega_O^2 a^4/32\mu_0 v_A$. This loss leads to a change in ‘Oumuamua’s spin energy $\sim \pi\rho_O c^2\omega_O^2 a^3/24$ such that its spin evolves on a timescale $\tau_\omega = \dot{\omega}_O/\omega_O \sim (16/3\sin^2\theta)(v_{\text{term}}/v_{d0})^2\tau_{d0}$, which is greater than a few Gyr. ISOs’ tumbling motion through magnetic fields (coupled to the turbulent interstellar medium) further lengthens τ_ω , so that the effect of Alfvén wave radiation does not significantly affect ‘Oumuamua’s spin frequency.

Vaporising H₂O ice by solar irradiation to provide the non-gravitational acceleration. Since other scenarios either require unrealistic physical properties or do not lead to sufficient thrust, outgassing is the most promising mechanism to account for ‘Oumuamua’s observed non-gravitational acceleration during its brief passage through the inner Solar System⁷. Moreover, the light curve of ‘Oumuamua can also be well reproduced with the consideration of the torque caused by outgassing⁴⁷. Upper limits put on the production rate of several molecular species of ‘Oumuamua rule out^{2,8,9,64} that the observed non-gravitational acceleration is driven by CN/C₂/C₃, CO₂/CO, and micron-size dust. Nevertheless, H₂O remains a viable source of outgassing and may potentially account for the non-gravitational forces^{7,65}. For an object with a mass of m , the acceleration generated from vaporising water ice is $a_{\text{H}_2\text{O}} = Q_{\text{H}_2\text{O}}\eta v_{\text{th}}/m$, where $Q_{\text{H}_2\text{O}}$ is the production rate of H₂O and v_{th}

is the gas thermal speed. The dimensionless efficiency factor η is largely affected by the geometry of the emission. With a porous surface⁴¹, the outgassing of H₂O molecules into vacuum is expected to be collimated towards the Sun⁶⁶ rather than in some random directions. The effective irradiated area is taken as the projected area that is normal to the solar irradiation direction such that $\eta \sim 1$. During the span of observation (from 2017 October 19 to 2018 January 2), the surface temperature of ‘Oumuamua varies from 350 K to 200 K with $v_{\text{th}} \simeq 300\text{--}400$ m/s. The observed non-gravitational radial acceleration of ‘Oumuamua is about $a_{\text{ng}} \sim 5 \times 10^{-6}(r/1 \text{ AU})^{-2} \text{ m s}^{-2}$. For a $200 \text{ m} \times 20 \text{ m} \times 20 \text{ m}$ ($a = 100 \text{ m}$ and $b = c = 10 \text{ m}$) prolate object with a bulk density of $1,000 \text{ kg m}^{-3}$, the required water sublimation production rate is $Q_{\text{H}_2\text{O}} \simeq ma_{\text{ng}}/v_{\text{th}} \sim 0.7 \text{ kg/s}$ at 1 AU.

Assuming the effective irradiated area for a tumbling prolate object is A_{eff} , which is the averaged projected area normal to the solar irradiation direction, the vapour production rate can be estimated by

$$Q'_{\text{H}_2\text{O}} = \left[\frac{(1-p)F_{\odot} - \epsilon\sigma T_{\text{sub}}^4}{\Delta H/N_A + \gamma k_B T_{\text{sub}}} \right] A_{\text{eff}} m_{\text{H}_2\text{O}},$$

where p is the surface albedo, F_{\odot} is the local integrated solar flux, ϵ is the bolometric emissivity, σ is the Stefan-Boltzmann constant, T_{sub} is the sublimation temperature, ΔH is the sublimation enthalpy, N_A is the Avogadro constant, γ is the heat capacity ratio, k_B is the Boltzmann constant, and $m_{\text{H}_2\text{O}}$ is the mass of one H₂O molecule. With $p = 0$, $F_{\odot} = 1367(r/1\text{AU})^{-2} \text{ W m}^{-2}$, $\epsilon = 0.95$, $T_{\text{sub}} = 144 \text{ K}$, $\Delta H = 54000 \text{ J/mol}$, $\gamma = 1.33$, and $A_{\text{eff}} = \pi ab$, the maximum production rate at 1AU is $\sim 1.37 \text{ kg/s}$. This value is comparable to the required water vapour production rate $Q_{\text{H}_2\text{O}}$ to account for the non-gravitational acceleration of ‘Oumuamua.

During the two months’ observations since ‘Oumuamua’s perihelion passage, the total outgassing amount of H₂O to produce the non-gravitational acceleration is $\sim 1.2 \times 10^6 \text{ kg}$. The water ice inventory between $\sim 0.1\text{--}0.2 \text{ m}$ and $\sim 0.4 \text{ m}$ that can commence sublimation during this period (see Fig. 3c), is sufficient to provide the required amount of H₂O. This amount is a few percent of M_O so that ‘Oumuamua’s mass and size were not significantly modified.

Nevertheless, a low production rate of water ice has been suggested for ‘Oumuamua based on its low observationally inferred carbon abundance and the C/O ratios of some Solar System

comets⁶⁷. If most of the volatile carbon-rich molecules have already sublimated and been ejected from ‘Oumuamua when it was in the proximity of its original host star (see section “Thermal modelling” in Methods), this constraint would be relaxed. Observations also indicate low C/O ratios in extrasolar planetesimals⁶⁸.

With a porous surface, dust production associated with the gas sublimation can also lead to outgassing with silicate-water ice composition. This additional source would enhance ‘Oumuamua’s non-gravitational acceleration. If the grains are predominantly larger than a few hundred micrometres to millimetres, they would not have been detected at optical wavelengths^{2,7,9,64}. Other volatile gases including N₂ and H₂ can sublimate at lower temperatures with lower sublimation enthalpy. They are also more likely to be severely depleted during the debris’ close encounter with their original host stars. Such propulsion fuel may need to be accreted onto ISOs during their voyage through the GMCs⁶⁹.

Asteroidal ISOs’ mass budget. Based on the sole detection of ‘Oumuamua during 3.5 yr operation of the Panoramic Survey Telescope and Rapid Response System (Pan-STARRS), the spacial density of asteroidal ISOs with ‘Oumuamua’s attributes is estimated^{10,11} to be $n_{\text{ISO}} \sim 3.5 \times 10^{13} - 2 \times 10^{15} \text{ pc}^{-3}$. The range reflects uncertainties on detection efficiency and Sun’s gravitational focusing effect.

There are potential candidates for ISOs’ original host stars in the solar neighbourhood. The average stellar mass⁷⁰ and number density¹¹ are $M_* \sim 0.37 M_{\odot}$ and $n_* \sim 0.32 \text{ pc}^{-3}$, respectively. In order to attain n_{ISO} , each star must eject, on average, $N_{\text{ej}} \simeq n_{\text{ISO}}/n_* \sim (1-60) \times 10^{14}$ asteroidal ISOs. Using ‘Oumuamua’s mass ($M_O \lesssim 10^8 \text{ kg}$ for $\rho_O = 1,000 \text{ kg m}^{-3}$, $a = 100 \text{ m}$, $b = c = 10 \text{ m}$) to normalise the ISOs’ average mass M_{ISO} , the required mass ejection per star is $M_{\text{ej}} = N_{\text{ej}} M_{\text{ISO}} \simeq (0.0017-0.1)(M_{\text{ISO}}/M_O) M_{\oplus}$, i.e., a fraction of the mass of the Moon or the Earth. Even for the upper limit, our estimate is two orders of magnitude less than some previous estimates¹⁰ because we use a smaller ISO mass normalisation factor M_O (than that of a sphere with $a = b = c = 100 \text{ m}$ and $\rho_O = 3,000 \text{ kg m}^{-3}$) and a larger n_* (relative to 0.1 pc^{-3}). The magnitude of M_{ej} would be further reduced if ‘Oumuamua’s small speed relative to the LSR (in comparison to the old field stars) leads to a local concentration of sub-km-sized ISOs.

We now compare M_{ej} with various potential reservoirs of their progenitors. *In situ* Solar

System formation scenario⁷¹ suggests a minimum mass $\sim 100M_{\oplus}$ of planetesimals within a few tens of AU. Similar mass values are estimated for protostellar disks. Since stars form in clusters with neighbours which perturb the outer ($\gtrsim 100$ – $1,000$ AU) disk regions, fractional loss of residual planetary building blocks is generally expected¹¹. However, the detached planetesimals from these regions are mostly icy, similar to the long-period comets (LPCs). Without surface transformation due to heating during their close encounters with their host stars, the ejected objects become cometary ISOs, which may be the mechanism to eject the interstellar comet 2I/Borisov⁷² from its original planetary system.

During advanced stages of their growth, proto gas and ice giant planets scatter⁷³ a few M_{\oplus} of nearby residual planetesimals. A fraction of the outwardly scattered objects settle in the inner and outer Oort cloud (with orbital semi-major axes $\sim 2 \times 10^3$ – 2×10^4 AU and $\sim 2 \times 10^4$ – 2×10^5 AU, respectively) as LPCs. From the average mass¹³ ($M_{\text{comet}} \sim 4 \times 10^{13}$ kg) of individual LPCs and their estimated total number²¹ ($N_{\text{LPC}} \sim 10^{12}$), we infer a total mass $M_{\text{LPC}} = N_{\text{LPC}}M_{\text{comet}} \sim 7M_{\oplus}$ for the LPC population.

In comparison with required asteroidal ISOs to be ejected per star, $N_{\text{LPC}} \sim (0.00017$ – $0.01)N_{\text{ej}}$, $M_{\text{LPC}} \gtrsim (70$ – $4,000)M_{\text{ej}}$, because $M_{\text{comet}} \gtrsim 4 \times 10^5 M_{\text{O}}$. In order for the LPCs to evolve into sufficient number of ‘Oumuamua-like ISOs, they need to be efficiently scattered to the proximity of the host star and substantially downsized analogous to comet Shoemaker-Levy-9. LPCs in the outer Oort cloud are loosely bound to the Sun whereas those stored in the inner Oort cloud are weakly perturbed by the combination of the Galactic tide, passing stars, gas and ice giant planets. These effects can lead to the loss of half of LPC population to the interstellar space over the Sun’s main sequence lifespan⁷⁴. They also lead to an infusion of LPCs to the Sun’s proximity²¹ at the observed rate of ~ 1 – 10 events per year^{75–77}.

Similar dynamical processes can also occur around lower-mass stars. Although they rarely bear gas giants, perturbations from the Galactic tides, field stars, ice giant planets, and super-Earths may have more intense influence on the dynamical evolution of residual planetesimals around lower-mass stars. Since $M_{\text{LPC}} \sim 100M_{\text{ej}}$, they have adequate supply of potential parent bodies for producing asteroidal ISOs by our hypothetical formation and ejection mechanism, even in the limit that the mass of their debris disk is proportion to their own mass.

As the host stars evolve off the main-sequence stage, the red-giant envelopes engulf planets and residual planetesimals within a few AU. While most of the outer major, dwarf, and minor planets are released to become freely floating planets and cometary ISOs, a fraction may be retained³⁰. The mass reduction of their hosts also promotes long-term orbital evolution^{29,78}, which may lead to close stellar encounters and tidal disruption. Many white dwarfs show signs of ongoing and active accretion of refractory elements^{51,79} at the rate of $\sim 10^5\text{--}10^6 \text{ kg s}^{-1}$. Over the white dwarfs’ cooling and dimming timescales, the integrated amount of mostly refractory elements accreted onto them⁵¹ is $\sim 0.001\text{--}0.1 M_{\oplus}$. If a similar amount of 100-m-sized tidal disrupted fragments are released from their host white dwarf, it would be comparable to the lower estimates for M_{ej} . However, parent bodies of asteroidal ISOs in this size range are preserved provided their $d_p \sim d_{\text{limit}}(100 \text{ m}) \sim 0.5 R_{\odot}$ (see “Tidal disruption limiting distance” in Methods). This requirement confines the formation domain around white dwarfs for the ‘Oumuamua-like asteroidal ISOs. Finally, the progenitors of white dwarfs are main-sequence stars with mass in the range $(0.8\text{--}8)M_{\odot}$. They are an order of magnitude less numerous than the lower-mass main-sequence stars. Nevertheless, they may provide the original host for a small fraction of the asteroidal ISOs with ‘Oumuamua’s attributes.

Tidal disintegration of super-Earths around low-mass stars. In the main text, we introduce the tidal disruption simulations of a self-gravity-dominated super-Earth (with $R_p = 2 \times 10^7 \text{ m}$ and $M_p = 11 M_{\oplus}$) on an $e_0 = 0.999$ and $d_p = 4 \times 10^8 \text{ m} < d_{\text{Roche}}$ orbit around a $0.5 M_{\odot}$ host star. In this case, half of the fragment, with mass up to $M_{\text{upper}} \sim 0.1 M_p$, can obtain a normalised orbital-energy-per-unit-mass increment $f_E \gtrsim 1$ and escape from the host star (see “Ejection condition” in Methods). The ejection of such large fragments provides a potential release mechanism for the freely floating super-Earths found by the microlensing observations⁸⁰. The retained fragments with eccentricity < 1 and mass $\lesssim M_{\text{upper}}$, come back for subsequent encounters and be ground down to smaller fragments. These later-generation fragments also contribute to the population of asteroidal ISOs. But, if multiple downsizing steps are needed, only a minute fraction of the initial M_p would be transformed into sub-km-sized asteroidal ISOs.

In Methods section “Tidal disruption limiting distance”, we show that the condition for tidal disruption is R_p -independent for large objects bound by gravity. But for small strength-dominated bodies, the magnitude of $d_{\text{limit}}(R_p)$ is an increasing function of R_p . In the limit that $d_{\text{Roche}} \gtrsim d_p \gtrsim$

R_s , the disintegration of planet-size objects continues to cascade until their fragments are reduced to the size R_p for which $d_{\text{limit}}(R_p) \sim R_s$. Smaller fragments preserve their integrity outside the stellar surface. Since $d_{\text{limit}}/R_s \propto M^{-2/3}$, the region where tidal disruption occurs is more extended around low- M_s stars.

We simulate the consequence of more intense tidal disruption with $d_p = 1.0, 1.2,$ and 1.5×10^8 m around a $M_s = 0.1M_\odot$ and $R_s \sim 0.1R_\odot$ main-sequence star whose $d_{\text{Roche}} \sim 4 \times 10^8$ m. Our results show that, for $d_p = 1.5 \times 10^8$ m, the largest fragments' mass $M_{\text{upper}} \sim 0.1M_p$. But, with $d_p = 1.0 \times 10^8$ m, the parent body breaks down to the numerical resolution limit with $M_{\text{upper}} \lesssim 6 \times 10^{-3}M_p$ (see Supplementary Fig. 6). The size distribution of the fragments almost matches its initial particles' size distribution. In order to overcome the indicative limitation on numerical resolution, we simulated tidal disruption of smaller (with $R_p = 10^5$ m, 10^4 m, and 10^3 m) parent bodies. When the cohesive material strength is neglected, the simulations give very similar results to the 2×10^7 m model (these simulations do include the shear strength, which is size-independent).

This powderization process ceases when the size of fragments enters the strength-dominated regime⁸¹. For illustration, we impose cohesion in simulations with $C = 10$ Pa using the same encounter condition. In this limit, the model with $R_p = 1$ km produces larger (a few hundred meter-size) fragments than the cohesion-free model. The required cohesive strength for preserving the integrity of a fragment can be estimated by

$$C \geq \frac{4\pi G R_p^2 \rho_p^2}{5} \left(\frac{\sqrt{3}M_s}{4\pi \rho_s d_p^3} - s \right).$$

Hundred-meter-sized fragments with $C \sim 50$ Pa can survive in this extreme strong tidal disruption event. This level of cohesive strength can be easily provided by the sintering bonds developed during the surface solidification shortly after the periastron passage⁴⁰. By this means, most of the escaped fragments should have a size in the range of dozen meters to hundred meters, one of which could be an 'Oumuamua analog.

We estimate the probability of producing asteroidal ISOs by the tidal downsizing of dwarf planets, super-Earths and ice giants. Most low-mass stars bear multiple super-Earths and sub-Neptunes with mass on the order of a few M_\oplus ($\sim 100M_{\text{ej}}$). The prospect of tapping these rich

reservoirs to match M_{ej} requires a few percent efficiency for the delivery of a single super-Earths (or high efficiency of delivering a single dwarf planet) to the proximity of each individual host star on a sufficiently high-eccentricity orbit. Some potentially efficient triggering mechanisms include close encounters with, secular or Lidov-Kosai resonances induced by their binary stellar and gas giant planetary companions or by perturbations from passing field stars^{11,22,25,82}.

Analogous to the Earth, Uranus, and Neptune, the molten cores of exoplanets probably contain little CO but a vast amount of water under some super-critical phases. Planetary fragments' water retention probability and outgassing efficiency under the condition of their formation and subsequent intrusion into the Solar System are poorly known. It is highly uncertain whether the mechanism we proposed for 'Oumuamua's non-gravitational acceleration can operate among the relics of molten planetary cores.

Data availability

The data that support the plots within this paper and other findings of this study are available from the corresponding author upon reasonable request.

Code availability

The code used for the thermal analyses is available from the corresponding author upon reasonable request. The PKDGRAV code with granular physics is not yet ready for public release - its details and validation have been presented in many previous studies and are available from the corresponding author upon reasonable request.

31. Gasc, S. et al. Change of outgassing pattern of 67P/Churyumov-Gerasimenko during the March 2016 equinox as seen by ROSINA. *Mon. Not. R. Astron. Soc.* **469**, S108–S117 (2017).
32. Leshner, C. E. & Spera, F. J. in *The Encyclopedia of Volcanoes* (eds Sigurdsson, H. et al.) 113–141 (Academic Press, Elsevier, Amsterdam, 2015).
33. Richardson, D. C., Quinn, T., Stadel, J. & Lake, G. Direct large-scale N -body simulations of planetesimal dynamics. *Icarus* **143**, 45–59 (2000).

34. Stadel, J. G. *Cosmological N-body Simulations and Their Analysis*. Ph.D. thesis, Univ. Washington (2001).
35. Schwartz, S. R., Richardson, D. C. & Michel, P. An implementation of the soft-sphere discrete element method in a high-performance parallel gravity tree-code. *Granul. Matter* **14**, 363–380 (2012).
36. Zhang, Y. et al. Creep stability of the proposed AIDA mission target 65803 Didymos: I. discrete cohesionless granular physics model. *Icarus* **294**, 98–123 (2017).
37. Zhang, Y. et al. Rotational failure of rubble-pile bodies: influences of shear and cohesive strengths. *Astrophys. J.* **857**, 15 (2018).
38. Chau, K. T., Wong, R. H. C. & Wu, J. J. Coefficient of restitution and rotational motions of rockfall impacts. *Int. J. Rock Mech. Min. Sci.* **39**, 69–77 (2002).
39. Jiang, M., Shen, Z. & Wang, J. A novel three-dimensional contact model for granulates incorporating rolling and twisting resistances. *Comput. Geotech.* **65**, 147–163 (2015).
40. Schwartz, S. R., Michel, P. & Richardson, D. C. Numerically simulating impact disruptions of cohesive glass bead agglomerates using the soft-sphere discrete element method. *Icarus* **226**, 67–76 (2013).
41. Poppe, T. Sintering of highly porous silica-particle samples: analogues of early Solar-System aggregates. *Icarus* **164**, 139–148 (2003).
42. Holsapple, K. A. & Michel, P. Tidal disruptions II: a continuum theory for solid bodies with strength, with applications to the Solar System. *Icarus* **193**, 283–301 (2008).
43. Ramírez, I. et al. The dissimilar chemical composition of the planet-hosting stars of the XO-2 binary system. *Astrophys. J.* **808**, 13 (2015).
44. Kalirai, J. S. et al. The masses of population II white dwarfs. *Astrophys. J.* **705**, 408–425 (2009).
45. Scheeres, D. J., Ostro, S. M., Werner, R. A., Asphaug, E. & Hudson, R. S. Effects of gravitational interactions on asteroid spin states. *Icarus* **147**, 106–118 (2000).

46. Belton, M. J. et al. The excited spin state of 1I/2017 U1 ‘Oumuamua. *Astrophys. J.* **856**, L21 (2018).
47. Mashchenko, S. Modelling the light curve of ‘Oumuamua: evidence for torque and disc-like shape. *Mon. Not. R. Astron. Soc.* **489**, 3003-3021 (2019).
48. Ďurech, J., Sidorin, V. & Kaasalainen, M. DAMIT: a database of asteroid models. *Astron. Astrophys.* **513**, A46 (2010).
49. Harris, A. W. Tumbling asteroids. *Icarus* **107**, 209–211 (1994).
50. Veras, D. Post-main-sequence planetary system evolution. *R. Soc. Open Sci.* **3**, 150571 (2016).
51. Chen, D.-C. et al. A power-law decay evolution scenario for polluted single white dwarfs. *Nature Astron.* **3**, 69–75 (2019).
52. Weissman, P. R. Cometary impacts with the Sun: physical and dynamical considerations. *Icarus* **55**, 448–454 (1983).
53. Hui, M.-T., & Knight, M. M. New insights into interstellar object 1I/2017 U1 (‘Oumuamua) from SOHO/STEREO nondetections. *Astron. J.* **158**, 256 (2019).
54. Spitzer, L. & Schwarzschild, M. The possible influence of interstellar clouds on stellar velocities. II. *Astrophys. J.* **118**, 106 (1953).
55. Holmberg, J., Nordström, B. & Andersen, J. The Geneva-Copenhagen survey of the Solar neighbourhood II. New *uvby* calibrations and rediscussion of stellar ages, the G dwarf problem, age-metallicity diagram, and heating mechanisms of the disk. *Astron. Astrophys.* **475**, 519–537 (2007).
56. Draine, B. T. *Physics of the Interstellar and Intergalactic Medium* (Princeton Univ. Press, 2011).
57. Bialy, S. & Loeb, A. Could solar radiation pressure explain ‘Oumuamua’s peculiar acceleration? *Astrophys. J.* **868**, L1 (2018).
58. Eubanks, T. M. High-drag interstellar objects and galactic dynamical streams. *Astrophys. J.* **874**, L11 (2019).

59. Heiles, C. & Crutcher, R. Magnetic fields in diffuse HI and molecular clouds. *Lect. Notes Phys.* **664**, 137–182 (2005).
60. Neubauer, F. M. Nonlinear standing Alfvén wave current system at Io: theory. *J. Geophys. Res.* **85**, 1171–1178 (1980).
61. Wang, D. & Karato, S.-i. Electrical conductivity of talc aggregates at 0.5 GPa: influence of dehydration. *Phys. Chem. Miner.* **40**, 11–17 (2013).
62. Laine, R. O., Lin, D. N. C. & Dong, S. Interaction of close-in planets with the magnetosphere of their host stars. I. Diffusion, ohmic dissipation of time-dependent field, planetary inflation, and mass loss. *Astrophys. J.* **685**, 521–542 (2008).
63. Rafikov, R. R., Gurevich, A. V. & Zybin, K. P. Inductive interaction of rapidly rotating conductive bodies with a magnetized plasma. *J. Exp. Theor. Phys.* **88**, 297–308 (1999).
64. Ye, Q.-Z., Zhang, Q., Kelley, M. S. P. & Brown, P. G. 1I/2017 U1 (‘Oumuamua) is hot: imaging, spectroscopy, and search of meteor activity. *Astrophys. J.* **851**, L5 (2017).
65. Park, R. S., Pisano, D. J., Lazio, T. J. W., Chodas, P. W. & Naidu, S. P. Search for OH 18 cm radio emission from 1I/2017 U1 with the Green Bank Telescope. *Astron. J.* **155**, 185 (2018).
66. Seligman, D., Laughlin, G. & Batygin, K. On the anomalous acceleration of 1I/2017 U1 ‘Oumuamua. *Astrophys. J.* **876**, L26 (2019).
67. Sekanina, Z. Outgassing as trigger of 1I/‘Oumuamua’s nongravitational acceleration: Could this hypothesis work at all? Preprint at <http://arxiv.org/abs/1905.00935> (2019).
68. Wilson, D. J., Gänsicke, B. T., Farihi, J. & Koester, D. Carbon to oxygen ratios in extrasolar planetesimals. *Mon. Not. R. Astron. Soc.* **459**, 3282–3286 (2016).
69. Sandford, S. A., Allamandola, L. J. & Geballe, T. R. Spectroscopic detection of molecular hydrogen frozen in interstellar ices. *Science* **262**, 400–402 (1993).
70. Chabrier, G. Galactic stellar and substellar initial mass function. *Publ. Astron. Soc. Pacif.* **115**, 763–795 (2003).

71. Hayashi, C., Nakazawa, K. & Nakagawa, Y. in *Protostars and Planets II* (eds Black, D. C. & Matthews, M. S.) 1100–1153 (1985).
72. Guzik, P. et al. Initial characterization of interstellar comet 2I/Borisov. *Nature Astron.* **4**, 53–57 (2019).
73. Zhou, J.-L. & Lin, D. N. C. Planetesimal accretion onto growing proto-gas giant planets. *Astrophys. J.* **666**, 447–465 (2007).
74. Hanse, J., Jílková, L., Portegies Zwart, S. F. & Pelupessy, F. I. Capture of exocomets and the erosion of the Oort cloud due to stellar encounters in the Galaxy. *Mon. Not. R. Astron. Soc.* **473**, 5432–5445 (2017).
75. Everhart, E. Intrinsic distributions of cometary perihelia and magnitudes. *Astron. J.* **72**, 1002–1011 (1967).
76. Francis, P. J. The demographics of long-period comets. *Astrophys. J.* **635**, 1348–1361 (2005).
77. Neslušan, L. The fading problem and the population of the Oort cloud. *Astron. Astrophys.* **461**, 741–750 (2007).
78. Raymond, S. N., Armitage, P. J., Veras, D., Quintana, E. V. & Barclay, T. Implications of the interstellar object 1I/ʻOumuamua for planetary dynamics and planetesimal formation. *Mon. Not. R. Astron. Soc.* **476**, 3031–3038 (2018).
79. Manser, C. J. et al. A planetesimal orbiting within the debris disc around a white dwarf star. *Science* **364**, 66–69 (2019).
80. Mróz P. et al. Two new free-floating or wide-orbit planets from microlensing. *Astron. Astrophys.* **622**, A201 (2019).
81. Guimarãess, A. H. F. et al. Aggregates in the strength and gravity regime: particles sizes in Saturn’s rings. *Icarus* **220**, 660–678 (2012).
82. Wu, Y. & Lithwick, Y. Secular chaos and the production of hot Jupiters. *Astrophys. J.* **735**, 109 (2011).